Volume 9
Number 24
28 June 2021
Pages 4765–4982

Journal of Materials Chemistry B

Materials for biology and medicine

rsc.li/materials-b

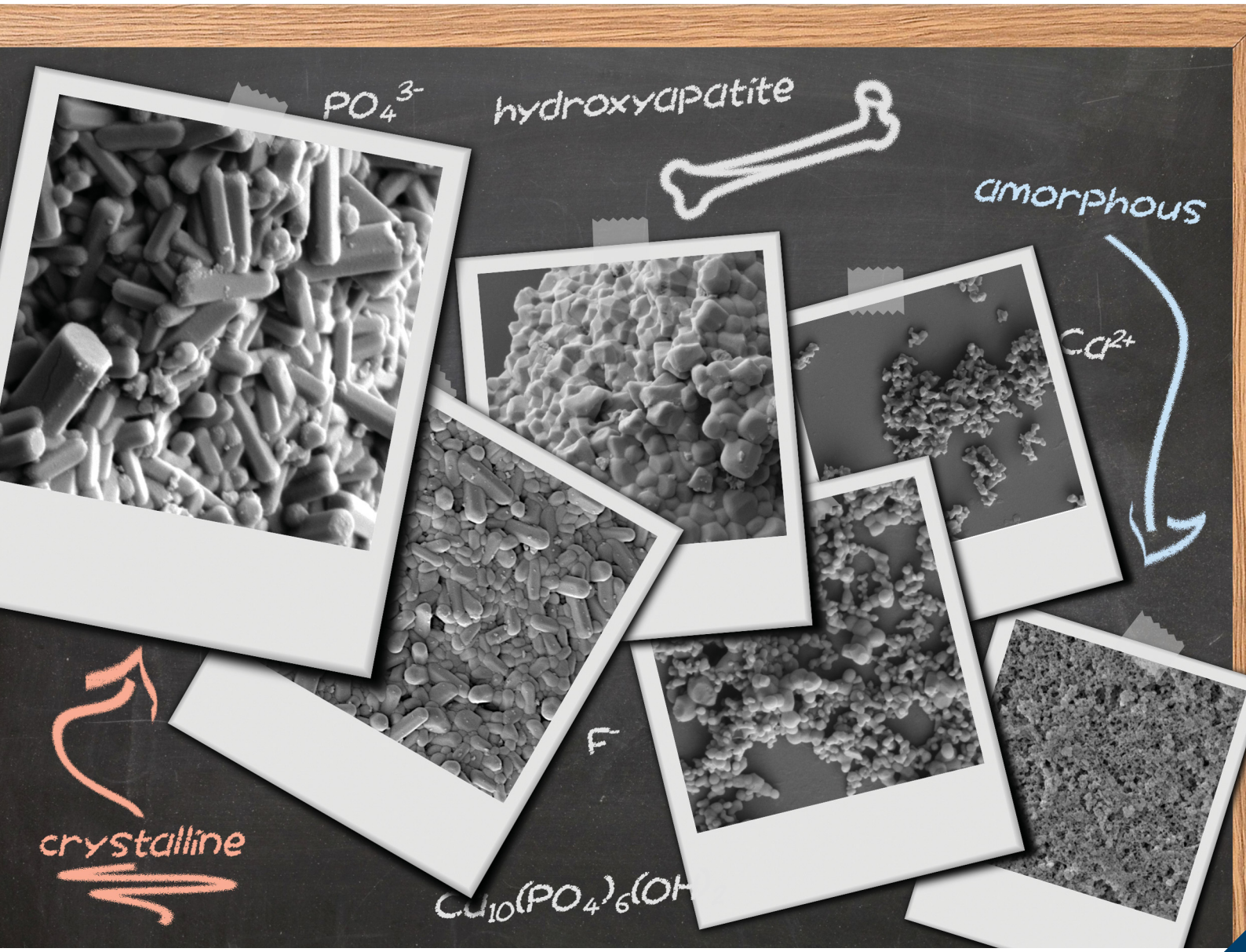

ISSN 2050-750X

ROYAL SOCIETY OF CHEMISTRY

PAPER

Lorenzo Degli Esposti, Michele Iafisco *et al.*
Thermal crystallization of amorphous calcium phosphate combined with citrate and fluoride doping: a novel route to produce hydroxyapatite bioceramics

Indexed in Medline!

Journal of Materials Chemistry B

ROYAL SOCIETY OF CHEMISTRY

PAPER

View Article Online
View Journal | View Issue

Cite this: J. Mater. Chem. B, 2021, 9, 4832

Thermal crystallization of amorphous calcium phosphate combined with citrate and fluoride doping: a novel route to produce hydroxyapatite bioceramics†

Lorenzo Degli Esposti, *[a] Smilja Markovic, [b] Nenad Ignjatovic, [b] Silvia Panseri,[a] Monica Montesi,[a] Alessio Adamiano,[a] Marco Fosca,[c] Julietta V. Rau, [cd] Vuk Uskoković [e] and Michele Iafisco *[a]

Amorphous calcium phosphate (ACP) is a material of high interest for dentistry, orthopedics, and other biomedical sectors. Being intrinsically metastable, the process of transformation of ACP into a crystalline phase upon heating is of high relevance for the development of innovative bioceramics. Here we have first studied the thermal behavior of a citrate-stabilized ACP (Cit-ACP) also doped with fluoride ions (Cit-FACP) prepared at three different nominal Cit/Ca ratios (*i.e.* 4, 2, 1) by differential thermal analysis. Next, the physico-chemical features of the crystalline products as well as the *in vitro* cell response to the materials were investigated. A citrate and fluoride free ACP sample was also tested as the blank. We have found that the activation energy of crystallization of Cit-(F)ACP samples is lower in comparison to the blank ACP and this is influenced by the nominal Cit/Ca molar ratio. Interestingly, we have discovered that the thermal treatment of Cit-(F)ACP at 800 °C yields hydroxyapatite (HA) or fluorapatite (FHA) as the main products differently from blank ACP that, like most of the ACPs reported in the literature, yields β-tricalcium phosphate. This was attributed to the Ca/P ratio of Cit-(F)ACP, which is similar to HA. A study of the crystalline products has revealed that all the (F)HA samples were non-cytotoxic, and retained carbonate ions in the crystal structure despite the heat treatment that should have induced decarbonation. The morphology of the products is influenced by the nominal Cit/Ca ratio and the presence of fluoride, ranging from spherical nanoparticles to micrometric hexagonal rods. Overall, our results prove that the thermal crystallization of Cit-(F)ACP is markedly different from classic ACP based materials and the thermal treatment of Cit-(F)ACP represents an attractive route for producing pure bioactive HA ceramics.

Received 19th March 2021,
Accepted 26th April 2021

DOI: 10.1039/d1tb00601k

rsc.li/materials-b

Introduction

Amorphous calcium phosphate (ACP) nanoparticles are one of the most interesting and promising classes of nanomaterials for biomedical application.[1,2] The structural unit of ACP first proposed by Betts and Posner[3,4] and later confirmed by high resolution imaging techniques,[5] is a spherical cluster with a diameter of *ca.* 9.5 Å with the structure of $Ca_9(PO_4)_6$. Betts and Posner suggested that ACP particles are composed of random aggregates of these so-called Posner's clusters, where water molecules, corresponding to *ca.* 20 wt%, "glue" the clusters to yield the $Ca_9(PO_4)_6{\cdot}nH_2O$ (where n is between 3 and 4.5) stoichiometry.[6] The Ca/P molar ratio of Posner's clusters is 1.5, but there are reports of several ACPs with different Ca/P molar ratios, which are believed to possess different local arrangements of atoms.[1,7] ACP can also incorporate other ions as substituents for Ca^{2+} and PO_4^{3-} ions, which in turn influence the Ca/P molar ratio.[8,9] Interestingly, the spatial arrangement of Ca^{2+} and PO_4^{3-} ions in the Posner's cluster is very similar to some regions of hydroxyapatite (HA, $Ca_{10}(PO_4)_6(OH)_2$), octacalcium phosphate (OCP, $Ca_8H_2(PO_4)_6{\cdot}5H_2O$), and tricalcium phosphate (TCP, $Ca_3(PO_4)_2$) unit cells, for which reason the transformation of

[a] Institute of Science and Technology for Ceramics (ISTEC), National Research Council (CNR), Via Granarolo 64, 48018 Faenza, Italy. E-mail: lorenzo.degliesposti@istec.cnr.it, michele.iafisco@istec.cnr.it
[b] Institute of Technical Sciences of the Serbian Academy of Science and Arts, Knez Mihailova 35/IV, P. O. Box 377, 11000 Belgrade, Serbia
[c] Institute of Structure of Matter (ISM), National Research Council (CNR), Via del Fosso del Cavaliere 100, 00133 Rome, Italy
[d] Sechenov First Moscow State Medical University, Institute of Pharmacy, Department of Analytical, Physical and Colloid Chemistry, Trubetskaya 8, Build. 2, 119991 Moscow, Russia
[e] TardigradeNano LLC, Irvine, CA, 92604, USA

† Electronic supplementary information (ESI) available. See DOI: 10.1039/d1tb00601k

ACP into all these crystalline phases is thermodynamically favored.[10,11] ACP is intrinsically metastable and given sufficient time, temperature and/or humidity, it will crystallize into one of the aforementioned calcium phosphate phases. Indeed, ACP is of high biological relevance because it is the precursor of biogenic HA of bones and teeth.[12–15] It was demonstrated by Robinson *et al.*[16] and Beniash *et al.*[17] that the mineralization of tooth enamel occurs through the deposition of spherical ACP nanoparticles into chains that crystallize to HA, and a similar mechanism was also proposed for bone formation.[18]

Apart from their biological relevance, ACP nanoparticles were extensively studied as remineralizing agents in dentistry and as biomaterials for bone repair.[1,2] They are used, for example, in remineralizing toothpastes, coatings for prostheses, self-setting injectable cements, and hybrid composites.[1,2,15] All these applications rely on the capacity of ACP to crystallize and form HA in the presence of water, similarly to the biogenic formation of HA. Therefore, the transformation of ACP into one or more crystalline phases is an intriguing process and is of great relevance for any ACP-related applications. The most studied crystallization process for ACP is the water-mediated one;[19] however, heating in vacuum or air can also induce crystallization.[8,20] Upon heating, several transitions occur in ACP, starting from the irreversible loss of structural water and concluding with the transformation to a crystalline phase between 500 and 800 °C. The thermally induced crystallization of ACP usually produces the α- or β-polymorph of TCP.[1,2] This process is mainly controlled by a solid-state lattice reordering mechanism, where the $Ca_9(PO_4)_6$ stoichiometry of ACP leads to the formation of the crystal phase with the same stoichiometry (*i.e.* TCP).[6,21] ACP based materials with different compositions or Ca/P molar ratios were found to produce mixtures of TCP with other calcium phosphate phases (*e.g.* HA, α- + β-TCP mixtures, and calcium pyrophosphates, ordered in decreasing Ca/P ratio).[2,6,8,20,22–30] Apart from a few reports that will be discussed further,[8,25,31–34] the typical thermal crystallization of ACP does not yield a pure crystalline HA phase.

Several methods have been reported for preparing ACP, with the most common ones being wet precipitation in aqueous and non-aqueous solvents, quenching of molten calcium phosphates, high-energy mechanochemical synthesis, and sol–gel synthesis.[1,2] The main disadvantage of ACP is its instability, which makes its handling and preservation challenging and is a hindrance to its wide-scale application. Indeed, ACP rapidly crystallizes, not only in wet conditions, but also in the dry state.[19] Therefore, several additives and ions were studied to stabilize ACP.[35,36] The strong interaction of citrate with calcium phosphates was extensively studied in the past.[37] Recently we have developed a stable carbonate-doped ACP nanomaterial functionalized with citrate ions (Cit-ACP) that can also be doped with fluoride ions (Cit-FACP).[38] We have discovered that citrate successfully stabilizes ACP nanoparticles, making their amorphous structure steady for years in the dry state under atmospheric conditions.[38] Furthermore, we have found out that citrate allows one to tune specific properties of the final material by regulating the specific surface area, and that fluoride ions can be successfully delivered to tooth enamel when this material is used as a remineralizing agent in dentistry.[38] Indeed, *in vitro* experiments have proven that Cit-ACP and Cit-FACP nanoparticles are able to attach onto HA crystals of human enamel and dentin and to form a new mineral phase contiguous to the biogenic one, restoring the demineralized tissue into its native structure.[38]

The main aim of this work is the study of the thermal behavior of Cit-ACP and Cit-FACP nanoparticles and the evaluation of the crystalline products upon heating. The thermochemical parameters of Cit-ACP and Cit-FACP crystallization have been characterized with the use of differential thermal analysis and modeled kinetically, while the physico-chemical features of the crystalline products as well as the *in vitro* cell response to the materials were investigated.

Experimental

Materials

Calcium chloride dihydrate ($CaCl_2{\cdot}2H_2O$, ≥99.0% pure), 3-(4,5-dimethylthiazol-2-yl)-2,5-diphenyltetrazolium bromide (MTT, ≥97.5% pure), hydrochloric acid (HCl, ≥37.0% pure), dimethyl sulfoxide (DMSO, ≥99.5% pure), sodium citrate tribasic dihydrate ($Na_3(C_6H_5O_7){\cdot}2H_2O$, ≥99.0% pure, hereafter called Na_3(Cit)), sodium phosphate dibasic dihydrate ($Na_2HPO_4{\cdot}2H_2O$, ≥99.0% pure), sodium carbonate monohydrate ($Na_2CO_3{\cdot}2H_2O$, ≥99.0% pure), sodium fluoride (NaF, ≥99.0% pure), paraformaldehyde (≥95.0% pure), phosphate buffered saline (PBS, 1× solution), and *t*-octylphenoxypolyethoxyethanol (Triton X-100, laboratory grade) were purchased from Sigma Aldrich (St. Louis, MO, USA). 4′,6-Diamidino-2-phenylindole dihydrochloride (DAPI, ≥95.0% pure), fetal bovine serum (FBS), fibroblast growth factor basic (FGFb, ≥95.0% pure), fluorescein-5-isothiocyanate-conjugated phalloidin (FITC-conjugated phalloidin, ≥90.0% pure) and penicillin–streptomycin (1000 U mL^{-1}) were purchased from Invitrogen (Waltham, MA, USA). Minimum essential medium α (αMEM) was purchased from Gibco (Gaithersburg, MD, USA). All the solutions were prepared with ultrapure water (18.2 MΩ cm, 25 °C, Arium© pro, Sartorius).

Sample preparation

Cit-ACP samples were synthesized as reported by Iafisco *et al.*[38] Cit-ACP was prepared by mixing at room temperature two aqueous solutions, consisting of (i) 100 mL of 100 mM $CaCl_2$ + *X* mM Na_3(Cit) (where *X* = 100 for Cit-ACP-1, 200 for Cit-ACP-2, and 400 for Cit-ACP-4) and (ii) 100 mL of 120 mM Na_2HPO_4 + 200 mM Na_2CO_3. After mixing, the pH was brought to 8.5 with concentrated HCl and after precipitation the particles were collected by centrifugation (7000 rpm, 5 min, 4 °C) and repeatedly washed with ultrapure water. Finally, the materials were freeze-dried overnight. Cit-FACP samples were prepared with the same procedure of Cit-ACPs, but with the addition of 50 mM NaF to solution (ii). Below in the text, Cit-ACP and Cit-FACP will be defined together as Cit-(F)ACP.

Citrate-free ACP (thereafter called blank-ACP) used as the reference material was synthesized by slightly modifying the

wet chemical precipitation reported by Onuma *et al.*[39] Blank-ACP was prepared by mixing at 4 °C two solutions, consisting of (i) 100 mL of 20 mM $CaCl_2$ and (ii) 100 mL of 20 mM Na_2HPO_4, and the precipitate was washed three times by centrifugation (12 500 rpm, 4 min, 4 °C), the first two with cold water and the last with a solution of ethanol–water (70 : 30 v/v), and then freeze-dried.

Thermal treatment of bulk powders

The amorphous samples were calcined above their crystallization temperature to obtain and then characterize their crystallization products. About 400 mg of powdered samples were put in an alumina crucible and heated in a static oven (KL40/12, Nannetti, Faenza, Italy) from room temperature to 800 °C at a heating rate of 100 °C h^{-1}, and then left to spontaneously cool down. Afterwards, the obtained powders were manually ground to uniform granularity.

Chemical, morphological, and structural characterization

Powder X-ray diffraction (PXRD). PXRD patterns of the samples were recorded on a D8 Advance diffractometer (Bruker, Karlsruhe, Germany) equipped with a Lynx-eye detector using Cu Kα radiation (λ = 1.54178 Å) generated at 40 kV and 40 mA. PXRD patterns of as-prepared and calcined ACP samples were collected in the 10–60° 2θ range with a step size of 0.02 degree and a collection time of 0.5 s. For calcined samples, HA unit cell parameters were calculated by Rietveld refinement considering a single- or multi-phase system, using tabulated atomic coordinates of HA, FHA, and CaO (HA: PDF card 00-009-0432, FHA: PDF card 00-015-0876, CaO: PDF card 00-037-1497)[40,41] with the software TOPAS5.[42]

Fourier transform infrared spectroscopy (FT-IR). FT-IR spectra were collected on a Nicolet 5700 spectrometer (Thermo Fisher Scientific Inc., Waltham, MA, USA) with a resolution of 2 cm^{-1} by accumulation of 32 scans covering the 4000 to 400 cm^{-1} range, in ATR mode using ATR iD7 accessory.

Elemental quantification. Ca and P content of the samples was measured by inductively-coupled plasma optical emission spectrometry (ICP-OES) using an Agilent 5100 (Agilent Technologies, Santa Clara, CA, USA), while F content was measured with an ion-selective electrode for fluoride (ISEF) Intellical ISEF121 (Hach Lange, Loveland, CO, USA). Before analysis, 10 mg of the powdered sample were dissolved in 50 mL of a 1 wt% HNO_3 aqueous solution.

Specific surface area analysis (SSA_{BET}). The specific surface area of the samples was measured through a N_2 gas adsorption method using a Sorpty 1750 instrument (Carlo Erba, Milan Italy) and Brunauer–Emmett–Teller (BET) approach.

Thermal characterization. The thermal behavior of the samples was studied by simultaneous thermogravimetric–differential thermal analyzer (TG–DTA) (SETSYS Evolution, SETARAM Instrumentation, Cailure, France). The samples were placed in Al_2O_3 crucibles (100 mL); an empty crucible was used as a reference. The heating profile was set as follows: both crucibles (reference and sample) were stabilized at 30 °C for 5 min then heated to 1000 °C, with heating rates of 5, 10, 20 and 50 °C min^{-1}, while the air flow was 20 mL min^{-1}. A baseline run was performed using empty crucibles under the same conditions, whereas baseline subtraction was carried out by CALISTO PROCESSING software equipped by SETARAM Instrumentation.

Energy dispersive X-ray diffraction coupled with heating chamber (EDXRD). EDXRD patterns were collected with an apparatus containing a commercial W-anode X-ray tube able to generate radiation up to 50 keV. Diffracted signals are collected by an EG&G high purity germanium photodiode whose energy resolution is about 1.5–2.0% in the 20–50 keV range. The EDXRD apparatus was coupled with a custom high-temperature cell with a feedback control and a dome-shaped beryllium window. This system allows us to perform high temperature measurements (up to 800 °C). The EDXRD patterns of the samples at 25 °C, 400 °C, and 700 °C were collected with an energy of 50 keV and current of 30 mA.

Scanning electron microscopy (SEM). SEM micrographs of calcined samples were acquired with a field-emission gun SEM microscope (FEG-SEM SIGMA, ZEISS NTS Gmbh, Oberkochen, Germany). Powdered samples were dispersed in water at a concentration of 0.1 mg mL^{-1}, followed by 10 min of sonication with a bath sonicator (Labsonic LBS1, FALC, Treviglio, Italy). Afterward, the particle dispersion was dropped on a silicon wafer mounted on a stub and left to dry at room temperature. The samples were then coated with 2 nm of Pt/Pd (80 : 20) alloy with a Polaron E5100 sputter-coater (Polaron Equipment, Watford, Hertfordshire, UK). Micrographs were acquired in secondary electron acquisition mode using an acceleration voltage of 3 kV.

Thermal data analysis

The Kissinger kinetic model was employed to calculate the activation energy (E_a) of the crystallization reaction. Specifically, in the model it is assumed that the crystallization rate coincides with the exothermic reaction peak in DTA, and thus the Kissinger model correlates the heating rate (β, K min^{-1}) with the peak temperature (T_p) of crystallization, allowing E_a to be calculated from eqn (1), where R is the gas constant:

$$\ln\left(\frac{\beta}{T_p^2}\right) = -\frac{E_a}{R \times T_p} + \text{constant} \quad (1)$$

For that purpose, four different heating rates, β were used: 5, 10, 20 and 50 °C min^{-1}. In addition, DTA data was also modeled with a variant of the Johnson–Mehl–Avrami–Kolmogorov model to derive the Avrami exponent for the solid-state reaction. Eqn (2) was used, where x was the degree of transformation ($x = S_T/S_0$), t is the reaction time in seconds, S_0 is the total integrated peak intensity and S_T is the integrated peak intensity at a temperature T:

$$\ln\left(\ln\left(\frac{1}{1-x}\right)\right) = n\ln(t) + n\ln(k) - \ln(2.3) \quad (2)$$

Plots depicting $\ln(\ln(1/(1-x)))$ as a function of $\ln(t)$ allowed us to calculate the Avrami exponent, n, from the slope. Integrated peak intensities were calculated using a manual multiple peak-fitting Gaussian routine (OriginPro 2018) on background-subtracted DTA diagrams of samples heated at a speed of 10 °C min^{-1}.

Biological characterization of calcined powder samples

Cell culture. Human Adipose-Derived Mesenchymal Stem Cells (MSCs) were purchased from ATCC (Manassas, VA, USA) and cultured following the company indications. MSCs were seeded at 2.5×10^3 cells per cm^2 and cultured in basal growth medium αMEM supplemented with 15% FBS, 1% penicillin–streptomycin (100 U mL^{-1}/100 μg mL^{-1}), and 10 ng mL^{-1} FGFb. 24 hours after the cell seeding, different concentrations of the powder samples (50 μg mL^{-1}, 100 μg mL^{-1}, 200 μg mL^{-1} and 500 μg mL^{-1}), which were sterilized by 25 kGy γ-ray radiation prior to use, were added and the cells were left in culture for 7 days. The cells grown in standard conditions without samples (named hereafter "cells only") were used as a control.

Evaluation of MSC viability. Quantitative cell viability and proliferation analysis were performed *via* MTT assay. In detail, MTT reagent was firstly dissolved in PBS 1× (5 mg mL^{-1}). The cells grown with and without the samples were incubated with 10% well-volume MTT solution for 2 hours at 37 °C and 5% CO_2 atmosphere conditions. The culture medium was then removed, substituted by DMSO and incubated for 15 min. In the assay, the metabolically active cells react with the tetrazolium salt of the MTT reagent to produce formazan crystals then dissolved by DMSO. The absorbance, read at λ_{max} of 570 nm, using a Multiskan FC Microplate Photometer (Thermo Fisher Scientific Inc., Waltham, MA, USA), is directly proportional to the number of metabolically active cells. For each type of sample and for the cells only three replicates were analyzed at 1, 3 and 7 days of culture. The results represent the % of viable cells with respect to the cells only and are expressed in graphs as mean ± standard error of the mean. Statistical analysis was made by two-way ANOVA analysis of variance followed by Tukey's multiple comparisons test by the GraphPad Prism software (version 6.0), with the statistical significance set at $p \leq 0.05$.

Cell morphology evaluation. After 2 days of culture, cell cultures were washed in 1× PBS for 5 min, fixed in 4% (w/v) paraformaldehyde for 15 min and permeabilized with 0.1% (v/v) Triton X-100 for 5 min. 38 nM FITC-conjugated phalloidin was added for 20 min at room temperature in the dark and DAPI 300 nM for 7 min was used for nuclear staining. Images were acquired by an Inverted Ti-E fluorescence microscope (Nikon).

Results and discussion

Structural and compositional characterization of the thermally untreated amorphous samples

Cit-(F)ACP samples were prepared at three nominal Cit/Ca molar ratios, *i.e.*, Cit/Ca = 1, 2 and 4, corresponding to Cit-(F)ACP-1, Cit-(F)ACP-2 and Cit-(F)ACP-4, respectively. All Cit-(F)ACP samples are amorphous, as previously demonstrated by the presence of only one broad reflection centered at *ca.* 30° 2θ in the PXRD patterns.[38] Blank-ACP displays a similar pattern (Fig. 1A), corroborating its amorphous state. The long-term stability of dry Cit-(F)ACP samples as amorphous materials shown in our previous work[38] and ascribed to the presence of citrate ions was further confirmed since the PXRD patterns of the samples collected after four years of storage at room temperature (Fig. 1B and C) are identical to those immediately after preparation. In contrast, blank-ACP powder converts spontaneously into crystalline HA in a matter of hours under ambient conditions (Fig. 1A).[2]

Chemical composition and SSA_{BET} of the samples are reported in ref. 38 and for the sake of clarity also in Table 1. All Cit-(F)ACP samples have comparable amounts of calcium, phosphate, citrate, and carbonate ions, and Cit-FACP samples also contain fluoride ions. Blank-ACP does not contain citrate and has a low amount of carbonate, the latter of which is due to atmospheric CO_2 dissolved in the solvent during precipitation. The Ca/P molar ratio of Cit-(F)ACP samples is remarkably higher than the Ca/P molar ratio of blank-ACP, and higher than the common value of 1.50 due to the presence of carbonate ions substituting for phosphates. This is supported by previous studies that have shown that the Ca/P ratio of ACP can be increased by incorporating high amounts of carbonate ions engaging in $PO_4 \rightarrow CO_3$ substitution.[8,34] The SSA_{BET} of the samples is in agreement with their nanometric nature, and the values reported for Cit-(F)ACP are remarkably higher in comparison to blank-ACP. For instance, Cit-(F)ACP samples have SSA_{BET} values that range from 200 up to 330 $m^2\ g^{-1}$, depending on the nominal Cit/Ca ratio, while the SSA_{BET} value of blank-ACP sample is 151 $m^2\ g^{-1}$. This latter value is similar to the SSA_{BET} of other ACPs reported in the literature, which are typically between 80 and 160 $m^2\ g^{-1}$.[43,44] The nominal Cit/Ca molar ratio does not influence the stability of Cit-(F)ACP in the dry state nor their structural and compositional features, but the SSA_{BET} changes significantly when the nominal Cit/Ca ratio

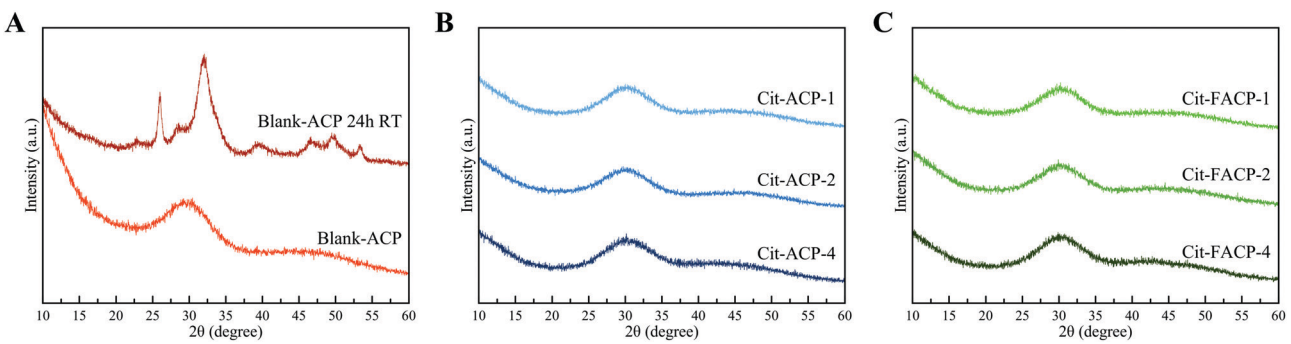

Fig. 1 PXRD patterns of (A) blank-ACP immediately after preparation and after 24 hours of storage at room temperature, (B) Cit-ACP and (C) Cit-FACP samples after 4 years of storage at room temperature.

Table 1 Chemical composition and specific surface area (SSA_{BET}) of the samples

Sample	Ca[a] (wt%)	P[a] (wt%)	F[b] (wt%)	Citrate[c] (wt%)	Carbonate[c] (wt%)	Ca/P (mol)	SSA_{BET}[d] ($m^2\ g^{-1}$)
Cit-ACP-4	29.9 ± 0.7[e]	13.6 ± 0.3[e]	—	1.9 ± 0.2[e]	3.7 ± 0.4[e]	1.70 ± 0.02[e]	200 ± 20[e]
Cit-ACP-2	29.1 ± 1.0[e]	13.2 ± 0.3[e]	—	2.2 ± 0.2[e]	3.8 ± 0.4[e]	1.70 ± 0.02[e]	287 ± 29[e]
Cit-ACP-1	28.0 ± 0.6[e]	12.7 ± 0.2[e]	—	1.8 ± 0.2[e]	3.2 ± 0.3[e]	1.70 ± 0.04[e]	309 ± 31[e]
Cit-FACP-4	31.4 ± 0.4[e]	13.6 ± 0.2[e]	1.00 ± 0.10[e]	1.5 ± 0.2[e]	3.8 ± 0.4[e]	1.78 ± 0.01[e]	213 ± 21[e]
Cit-FACP-2	32.1 ± 0.5[e]	13.1 ± 0.2[e]	1.10 ± 0.10[e]	2.0 ± 0.2[e]	3.4 ± 0.3[e]	1.89 ± 0.01[e]	328 ± 33[e]
Cit-FACP-1	31.9 ± 0.8[e]	13.1 ± 0.3[e]	1.30 ± 0.10[e]	2.4 ± 0.2[e]	3.1 ± 0.3[e]	1.88 ± 0.01[e]	293 ± 29[e]
Blank-ACP	28.8 ± 1.1	17.2 ± 0.7	—	—	0.8 ± 0.1	1.29 ± 0.01	151 ± 15

[a] Quantified by ICP-OES. [b] Quantified by ISEF. [c] Quantified by TGA. [d] Calculated from BET N_2 adsorption. [e] From Iafisco *et al.*[38]

was modified, independently from fluoride doping.[38] In particular, the two values are inversely proportional, where the SSA_{BET} increased when the nominal Cit/Ca ratio decreased. Previous studies have proven that citrate ions adsorb on the surface of ACP-forming nuclei,[45,46] minimizing their size and leading to the high values of SSA_{BET}. Therefore, the observed inverse proportionality between SSA_{BET} and the Cit/Ca ratio appears counterintuitive if the sole effect of citrate molecules on the dispersion of nuclei and crystallites in the system is presumed, meaning that other microstructural effects must be at work. The decrease of SSA_{BET} at higher Cit/Ca ratios could be attributed to an increment of the nucleation lag time with a consequent decrease of porosity. Another option is that the aggregation of ACP particles is responsible for the changes in SSA_{BET}, in which case citrate molecules could exhibit the concentration-dependent effect on particle–particle interaction. Indeed, surface additives are usually thought to hinder the surface processes at both low and high concentrations, but they also hamper the ionic diffusion only at high concentrations.[47] If a similar scenario applies to the role of citrate in the formation of Cit-(F)ACP particles, it could be possible that citrate slowed down the ionic diffusion at high Cit/Ca ratios, *e.g.*, Cit/Ca = 4, in comparison with Cit/Ca = 1, thus increasing the nucleation lag time,[48] which would correspond to the reduction of effective supersaturation and the growth of more fused and larger particles with a lower SSA.

Analysis of the thermal behavior of the amorphous samples

Thermally induced crystallization of Cit-(F)ACP was studied by DTA. In Fig. 2A, DTA curves of Cit-ACP samples together with blank-ACP are presented, while the corresponding TGA curves are reported in Fig. 2B. Cit-ACP and blank-ACP samples undergo three different thermal phenomena during heating. First, an endothermic event occurs at around 100 °C in parallel with a significant mass loss in the 30–200 °C range, which can be attributed to the vaporization of surface-bound and structural water, as is typical for ACP materials.[2] The area and the position of this peak is similar in all the samples, indicating a similar

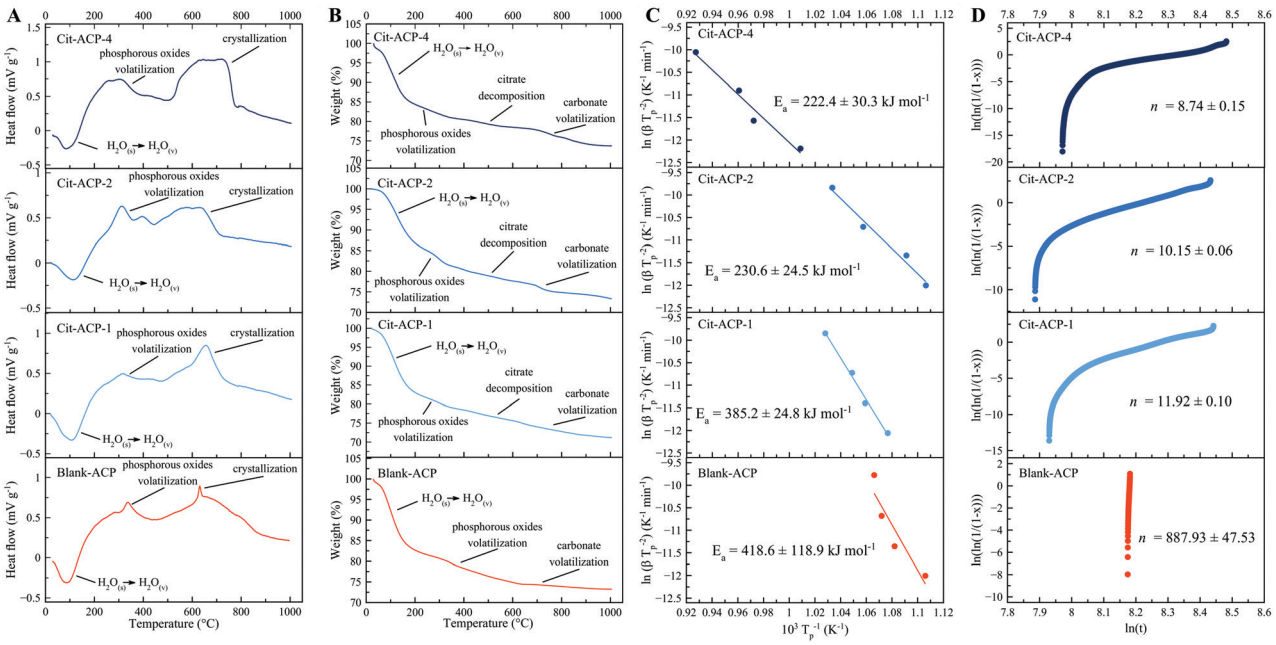

Fig. 2 (A) DTA and (B) TGA curves obtained by heating Cit-ACP-4, Cit-ACP-2, Cit-ACP-1, and blank-ACP powders at the rate of 5 °C min^{-1}. (C) Kissinger plots with corresponding E_a values and (D) Johnson–Mehl–Avrami–Kolmogorov curves with corresponding Avrami exponents n calculated from DTA curves.

hydration degree and bonding strength of water molecules. Second, an exothermic peak occurs at approximately 320 °C, with a corresponding small mass loss in the 200–400 °C range. This peak can be attributed to the heat-induced formation of volatile phosphorous oxides from phosphate and hydrogen phosphate groups.[6] Third, the thermally induced crystallization is identified by an exothermic peak in the 650–700 °C range, which is paired with two small mass losses in the 400–600 °C and 600–800 °C ranges due to the decomposition of adsorbed citrate ions and to the volatilization of carbonate ions, respectively. In the case of the blank-ACP sample, the 400–600 °C weight loss is not present, while the 600–800 °C mass loss is small, further confirming their attribution as citrate and carbonate decompositions, respectively. The crystallization exotherm progressively becomes more diffuse and spread over broader temperature ranges with an increase in the nominal Cit/Ca molar ratio (Cit-ACP-4 > Cit-ACP-1 > blank-ACP), indicating a greater polydispersity of physical states occupied by the amorphous units upon crystallization. Furthermore, the area of the crystallization peak increases as the nominal Cit/Ca ratio increases, indicating that the enthalpic gain during the phase transformation increases with the nominal content of citrate. Simultaneously, for all samples the crystallization peaks exhibit a shift to higher temperatures with an increase in the heating rate (Fig. S1A, ESI†). The rate of this shift was used to calculate the crystallization activation energies (E_a) using the Kissinger kinetic model.

The Kissinger curves show good fits (Fig. 2C), with the E_a being the highest for the blank-ACP sample (420 kJ mol^{-1}) and the lowest for Cit-ACP-4 (220 kJ mol^{-1}), while Cit-ACP-2 and Cit-ACP-1 take on intermediate values (230 and 385 kJ mol^{-1}, respectively). The E_a of blank-ACP is similar to the values previously reported in the literature for other ACP-based materials.[2,31] In detail, other works have estimated values of E_a at 450 kJ mol^{-1},[31] 435 kJ mol^{-1},[29] and about 500 kJ mol^{-1}.[49] Considering that the Kissinger model assumes that the concentration of nuclei remains constant throughout the crystallization process, the good fitting to the model indirectly confirms that the heat-activated crystallization follows a "martensitic" solid-state lattice reordering mechanism.[50] In addition, for Cit-ACP samples, there is a direct proportionality between the E_a and the SSA_{BET} values of the samples, which is a strong argument against the thermal crystallization of Cit-ACP as a surface-driven process and in favor of its proceeding through the internal lattice rearrangements. On the contrary, crystallization of Cit-ACP in aqueous physiological conditions was previously proved to be a surface-driven process regulated by the exchange of the ions of the Cit-ACP surface with those present in solution.[45] As can be seen in Fig. 2C and 4A, the E_a is not only notably lower in every Cit-ACP sample than in blank-ACP, but it also gets progressively lower as the nominal Cit/Ca ratio increases.

In addition, the Avrami exponent, n, was calculated from Johnson–Mehl–Avrami–Kolmogorov curves (Fig. 2D). This exponent is indicative of the mechanism of reaction, and it is inversely proportional to the nominal Cit/Ca ratio (Fig. 4B). This correlation may indicate that in Cit-ACP samples, especially for Cit-ACP-4, the crystallization process is less surface-controlled and more diffusion-controlled, which would agree with internal lattice rearrangement as the mechanism of crystallization. Another indication inferable from this correlation is that citrate lowers the degrees of freedom associated with the crystallization reaction, thus making it more streamlined. This correlation is also in agreement with the reduction of the E_a with the increase of nominal Cit/Ca ratio, which further suggests that the thermally induced crystallization becomes more spontaneous and, thus, more reliant on diffusion than on more complex kinetic, surface-related processes.

In Fig. 3A and B, the DTA and TGA curves for Cit-FACP samples are reported, which are similar to the curves for Cit-ACP samples. However, Cit-FACP-1 and Cit-FACP-2 samples present multiple exothermic peaks in the region between 300 and 600 °C, and the TGA diagrams corroborate this by showing a more step-like weight loss in this temperature range. This indicates a different behavior of Cit-FACP samples in comparison to Cit-ACP ones.

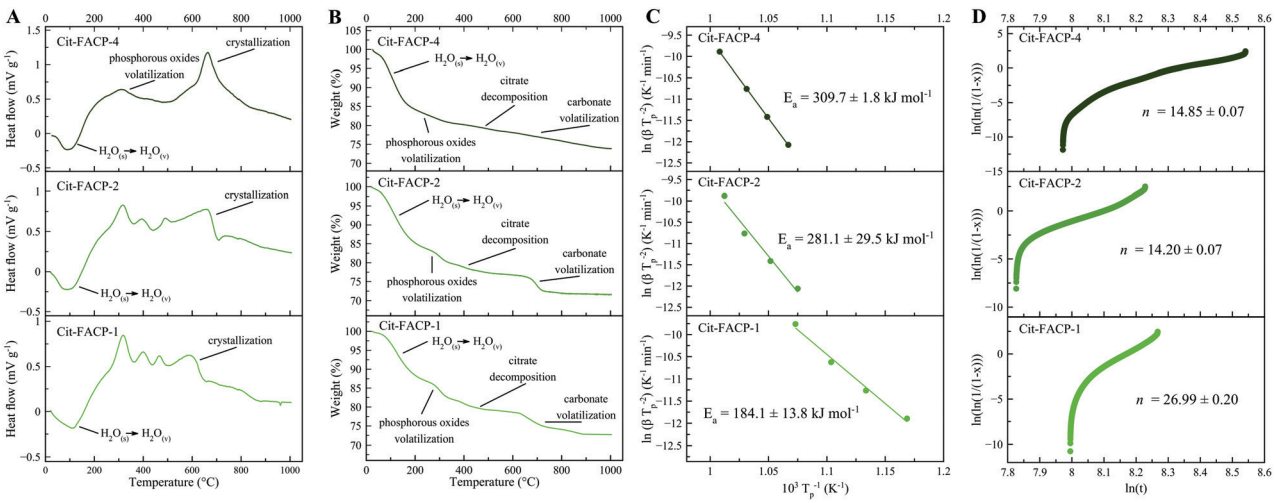

Fig. 3 (A) DTA and (B) TGA curves obtained by heating Cit-FACP-4, Cit-FACP-2, and Cit-FACP-1 powders at the rate of 5 °C min^{-1}. (C) Kissinger plots with corresponding E_a values and (D) Johnson–Mehl–Avrami–Kolmogorov curves with corresponding Avrami exponents n calculated from DTA curves.

Furthermore, for Cit-FACP samples, the crystallization exotherm becomes more diffuse and spread over broader temperature ranges with an increase in the nominal Cit/Ca molar ratio. The Kissinger curves calculated from the shift of the crystallization peak (Fig. S1B, ESI†) show good fits (Fig. 3C), and the E_a values (310 kJ mol^{-1}, 280 kJ mol^{-1}, 185 kJ mol^{-1} for CitFACP-4, Cit-FACP-2, and Cit-FACP-1, respectively) are directly correlated with the Cit/Ca ratio but are not clearly correlated with SSA_{BET}, in contrast to the trend observed for Cit-ACP samples (Fig. 2D and 4A).

Therefore, the relationship between Cit/Ca ratios and the E_a is more complex in fluoride-doped Cit-FACP samples. This is somewhat expected because fluoride is not only a component that affects the crystallization rate and mechanism,[51] but also the one that gets completely integrated inside the crystal lattice, unlike the citrate molecules. It is likely that for Cit-FACP samples the crystallization process is more surface-controlled than for Cit-ACP samples and the factors that influence crystallization E_a are therefore more complex. This hypothesis is also suggested by the higher Avrami exponents of Cit-FACP samples in comparison to Cit-ACP ones, which suggests a more surface-controlled process (Fig. 4B). Similarly to Cit-ACP, the Avrami exponent of Cit-FACP samples also decreases with the Cit/Ca ratio (Fig. 3E and 4B).

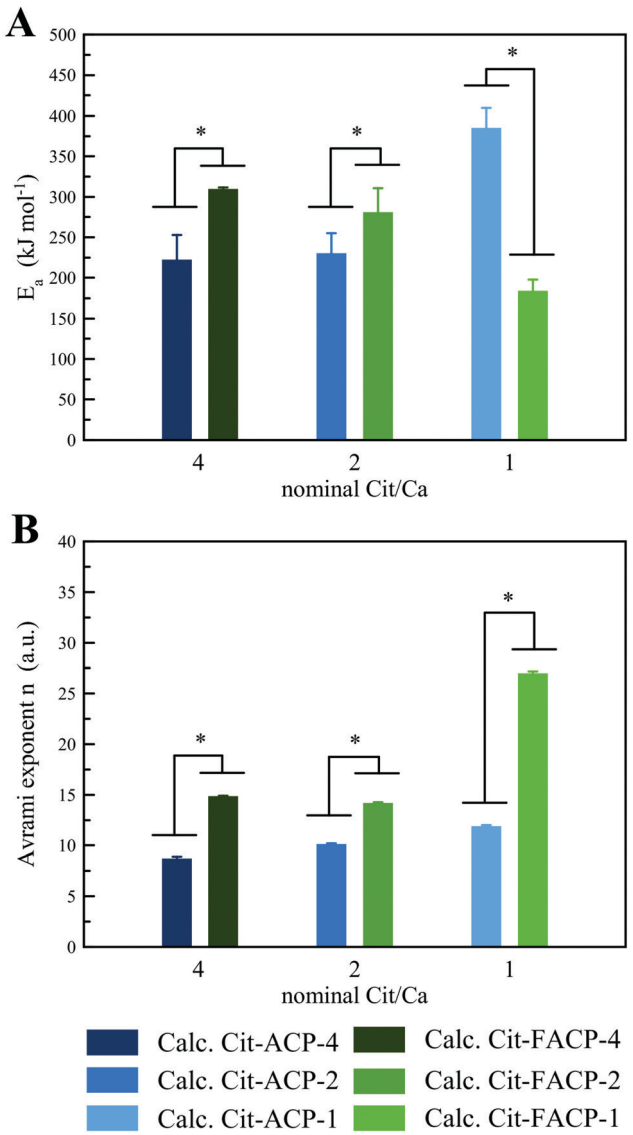

Fig. 4 Comparison between the (A) E_a and (B) Avrami exponent of crystallization of Cit-ACP and Cit-FACP samples at different nominal Cit/Ca ratios (*$p \leq 0.04$).

The transformation from amorphous to crystalline phase of Cit-(F)ACP samples was investigated by EDXRD. The EDXRD patterns of Cit-(F)ACP-4 and Cit-(F)ACP-1 stored at RT and heated at 400 °C and 700 °C are reported in Fig. 5. The patterns of the samples at 400 °C present small and broad diffraction peaks. Cit-ACP-1 and Cit-FACP-1 present a peak at 32° that is more defined in comparison to Cit-ACP-4 and Cit-FACP-4, where the latter two resemble more the pristine materials. This difference agrees with DTA data, where samples with a nominal Cit/Ca ratio of 1 have a sharper crystallization peak in comparison to the sample with a Cit/Ca of 4, for which the complete crystallization occurred over a larger temperature range. The patterns at 700 °C show a poorly crystalline product for all the samples, which was indexed as HA (PDF card file 00-009-0432). Overall, this result suggests that all Cit-(F)ACP materials crystallize into HA with heating.

Chemical, morphological, and biological characterization of crystalline materials obtained by the thermal treatment of the amorphous samples

Based on the above-reported findings, we next studied the crystallization products obtained by calcining the Cit-(F)ACP and blank-ACP powders. A calcination temperature of 800 °C was used, which is above the crystallization exotherm of all the samples.

The PXRD patterns of the calcined Cit-(F)ACP samples (Fig. 6) show that HA is the main product for all the samples. On the other hand, the PXRD pattern of calcined blank-ACP shows that there is no HA in the product, and all the peaks are attributed to γ-calcium pyrophosphate (γ-$Ca_2P_2O_7$) and to β-TCP. This mixture of crystal phases was previously reported for other calcined ACP samples.[26] Based on the broadness and the intensity of HA peaks, all the samples have a comparable crystallinity. Calcined Cit-ACP-4 is composed of pure HA, while the other Cit-(F)ACP samples present additional peaks at 37.4° and 53.9°, which are indexed as calcium oxide (CaO, PDF card file 00-037-1497). Semi-quantitative phase analysis through Rietveld refinement was performed (Table 2), showing that the CaO content is limited and remains below 1 wt% and 5 wt% for calcined Cit-ACP and Cit-FACP samples, respectively. Taking into account that Cit-FACP samples have a Ca/P molar ratio significantly higher than the Ca/P ratio of stoichiometric HA (*i.e.*, 1.67), it is likely that the excess in calcium reacts with atmospheric oxygen during thermal crystallization to form CaO, as occurs during the calcination of non-stoichiometric HA.[52,53]

The HA unit cell parameters of calcined samples are reported in Table 2. The *a*-cell parameter of Cit-FACP samples is *ca.* 0.3 Å shorter than that of Cit-ACP samples, while the *c*-unit cell

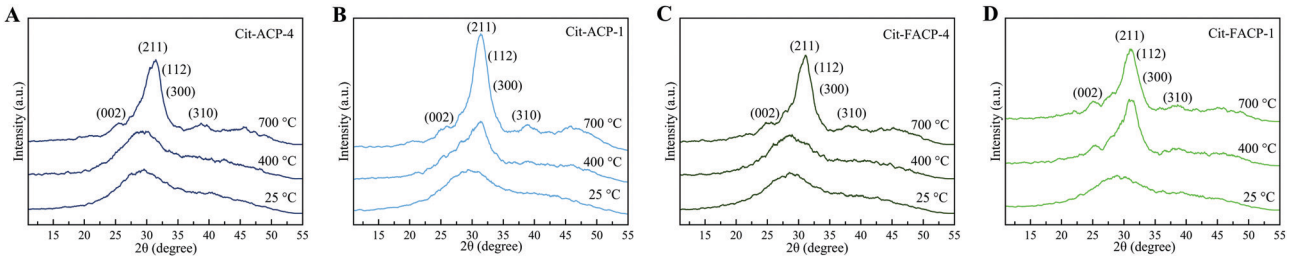

Fig. 5 EDXRD patterns of (A) Cit-ACP-4, (B) Cit-ACP-1, (C) Cit-FACP-4, and (D) Cit-FACP-1 at 25 °C, 400 °C, and 700 °C.

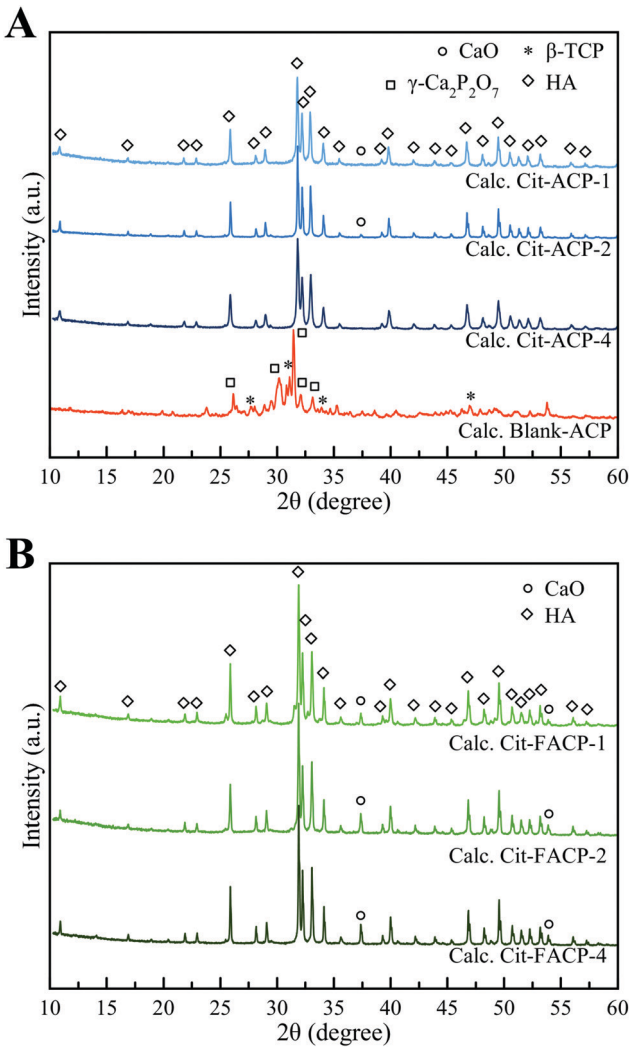

Fig. 6 PXRD patterns of calcined (A) blank-ACP, Cit-ACP-4, Cit-ACP-2, Cit-ACP-1, and (B) Cit-FACP-4, Cit-FACP-2, and Cit-FACP-1.

parameter is similar for both sets of materials. This difference indicates that the main phase of calcined Cit-FACP samples is fluorapatite (FHA, $Ca_{10}(PO_4)_6F_2$), since it is well reported in the literature that FHA possesses a slightly shorter *a*-cell axis than HA due to a shorter Ca^{2+}–F^- distance than that of Ca^{2+}–OH^-.[54–56]

The FT-IR spectra of calcined Cit-(F)ACP samples (Fig. 7) are in agreement with the PXRD patterns. Indeed, all Cit-(F)ACP samples present the typical bands of an apatitic phase. The main peaks correspond to the apatitic vibrational bands of phosphate groups: the symmetric stretching band ν_1PO_4 at *ca.* 960 cm^{-1}, the triply degenerated antisymmetric stretching band ν_3PO_4 at *ca.* 1025 cm^{-1} with a visible shoulder at 1090 cm^{-1}, and the triply degenerated bending band ν_4PO_4 at *ca.* 560 and 600 cm^{-1} with a shoulder at 575 cm^{-1}.[57] On the other hand, the calcined blank-ACP sample displays a completely different spectrum, confirming its structural difference in comparison to Cit-(F)ACP samples. This spectrum presents several bands that can be associated with the bending and the stretching of PO_4 groups at 450–650 cm^{-1} and 950–1150 cm^{-1}, respectively, which in turn are composed of several sub-bands that are due to the superposition of γ-calcium pyrophosphate and β-TCP vibrational modes. It can be observed that for all the samples, except for Cit-ACP-4, the ν_3PO_4 band is particularly broad. This has been described by Antonakos *et al.*[57] as an elongation of P–O bond lengths caused by the thermal decarbonation of crystalline HA, and was observed on carbonate-doped HA from natural sources calcined at high temperatures.[57,58] The broadening did not occur for Cit-ACP-4 because in this case the calcination temperature of 800 °C was not enough to alter the structure upon decarbonation.

Only crystalline Cit-ACP samples present the additional band at 628 cm^{-1}, which corresponds to the librational motion of apatitic hydroxyl ions (ν_LOH).[59] The absence of this band in crystalline Cit-FACP samples is further evidence of the formation of FHA, since this phase does not have a significant content of hydroxyl ions, which have been replaced by F^- ions.[55,60] Moreover, the calcined Cit-FACP samples possess a small band at *ca.* 720–740 cm^{-1}, which is due to the vibrational motion of the few OH^- ions trapped between F^- ions in FHA (νF-OH-F).[61]

Interestingly, the calcined Cit-(F)ACP samples present bands at *ca.* 870 cm^{-1} and in the region between 1350–1550 cm^{-1} that can be attributed to the ν_2CO_3 and ν_3CO_3 vibrations of the carbonate ion in an apatitic environment. This finding indicates that the calcination product is a carbonate-doped (F)HA. In particular, for all the samples, the bands peak at 870, 1411 and 1445 cm^{-1}, which is characteristic for a B-type carbonate substitution, where CO_3^{2-} substitutes PO_4^{3-} ions.[62] As expected, none of the samples presented the ν_3CO_3 band at *ca.* 1550–1600 cm^{-1}, indicating that citrate ions decomposed during heating, as shown by the results of the DTA analysis. The relative intensity of the ν_3CO_3 band in respect to the ν_3PO_4 band (I_{CO_3}/I_{PO_4}) is comparable for all the samples except for Cit-ACP-4, which is notably weaker. This indicates a lower carbonate content, as confirmed by the TGA data (see below).

Table 2 Phase composition and unit cell parameters of calcined samples

Sample	Composition		HA a–b cell axes (Å)	HA c cell axis (Å)
	HA (wt%)	CaO (wt%)		
Calc. Cit-ACP-4	100.0 ± 0.0	0.0 ± 0.0	9.416 ± 0.005	6.890 ± 0.005
Calc. Cit-ACP-2	99.0 ± 0.1	1.0 ± 0.1	9.420 ± 0.005	6.887 ± 0.005
Calc. Cit-ACP-1	99.7 ± 0.1	0.3 ± 0.1	9.421 ± 0.005	6.884 ± 0.005
Calc. Cit-FACP-4	95.6 ± 0.1	4.4 ± 0.1	9.385 ± 0.005	6.888 ± 0.005
Calc. Cit-FACP-2	95.4 ± 0.1	4.6 ± 0.1	9.384 ± 0.005	6.886 ± 0.005
Calc. Cit-FACP-1	97.9 ± 0.1	2.1 ± 0.1	9.386 ± 0.005	6.888 ± 0.005

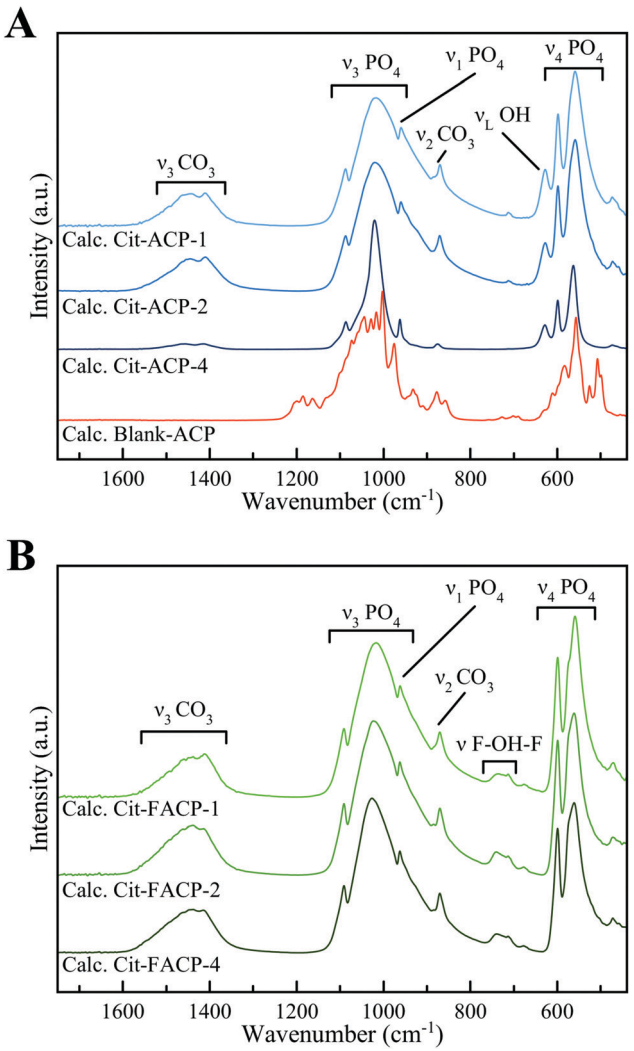

Fig. 7 FT-IR spectra of calcined (A) blank-ACP, Cit-ACP-4, Cit-ACP-2, Cit-ACP-1, and (B) Cit-FACP-4, Cit-FACP-2, and Cit-FACP-1.

The chemical composition of the crystalline samples is reported in Table 3. For all samples, the relative contents of Ca, P, and F are higher than those of their untreated counterparts, while the Ca/P ratio does not change. This confirms that upon calcination, the water and citrate molecules were removed without altering the chemical composition of the materials. In addition, the presence of fluoride in the Cit-FACP samples confirms the formation of FHA.

From these data, it is established that Cit-(F)ACP crystallizes into (F)HA without forming TCP. As noted earlier, upon heating, conventional ACP transforms into TCP because the thermal crystallization is controlled by a solid-state lattice reordering mechanism, and the basic ACP unit has a Ca/P ratio identical to TCP.[6,21] In this regard, the thermal crystallization of ACP into pure HA does occur, but based on literature reports, this has been achieved only in few specific conditions, explicitly in the cases of ACPs produced by plasma-spraying of HA,[31,32] by sol–gel synthesis,[25,33] or by wet precipitation in the presence of strong carbonate doping with a carbonate content higher than 4 wt%.[8,34] In the case of plasma-sprayed ACP, HA formation was thought to be derived from direct nucleation of the crystalline phase during the plasma spheroidization process,[31] meaning that the crystal phase selectivity was due to a seeding effect. In the other cases, HA was achieved only when the ACP has a Ca/P molar ratio identical to stoichiometric HA (1.67).[8,25,33,34] When the Ca/P ratio of ACP deviated from 1.67, a mixture of HA and TCP was obtained. Considering that Cit-ACP samples have a Ca/P ratio of 1.70, it is likely that in our case the formation of HA was due to the same effect.

Here, it must be taken into account that the production of ACP with the Ca/P ratio of 1.67 is not straightforward because this kind of ratio cannot be achieved by simple wet precipitation – the product inevitably has a Ca/P ratio of 1.50[6] – and more complex procedures are required, such as doping with high amounts of carbonate ions, or sol–gel syntheses. In our case, the simultaneous presence of citrate and carbonate ions in Cit-(F)ACP is an alternative method to achieve a Ca/P ratio of 1.67 and, therefore, to produce (F)HA by calcination.

Another peculiar trait of Cit-(F)ACP is that with calcination, the carbonate content decreases from *ca.* 3–4 wt% to *ca.* 2–3 wt%. This incomplete sublimation of the structural carbonates is an interesting finding, taking into account that the calcination temperature was within the thermal range in which decarbonation usually occurs (600–1000 °C).[63] As suggested by the results of the FT-IR analysis, not all of the carbonates were lost with calcination, which represents a remarkable result that will be investigated in more detail in our future studies. In fact, the obtainment of carbonate-doped ceramic HA is a notable achievement because carbonate-doped HA is more bioactive and resorbable than pure HA.[64] To the best of our knowledge, the currently used methods to sinter HA while preserving carbonate ions do not involve conventional heating procedures, such as sintering under CO_2 flow[63] or using spark plasma sintering.[9]

Table 3 Chemical composition of calcined samples

Sample	Ca[a] (wt%)	P[a] (wt%)	F[b] (wt%)	Citrate[c] (wt%)	Carbonate[c] (wt%)	Ca/P (mol)
Calc. Cit-ACP-4	36.3 ± 1.4	16.6 ± 0.5	—	—	0.4 ± 0.1	1.69 ± 0.01
Calc. Cit-ACP-2	39.3 ± 1.9	17.9 ± 0.9	—	—	2.5 ± 0.3	1.70 ± 0.02
Calc. Cit-ACP-1	36.8 ± 1.4	17.1 ± 0.6	—	—	2.1 ± 0.2	1.66 ± 0.01
Calc. Cit-FACP-4	37.6 ± 0.7	16.0 ± 0.2	2.0 ± 0.2	—	2.3 ± 0.2	1.82 ± 0.01
Calc. Cit-FACP-2	38.3 ± 0.5	16.3 ± 0.3	2.5 ± 0.1	—	1.7 ± 0.2	1.82 ± 0.02
Calc. Cit-FACP-1	36.9 ± 0.7	16.2 ± 0.4	2.1 ± 0.4	—	2.9 ± 0.3	1.76 ± 0.01
Calc. blank-ACP	35.7 ± 0.5	21.0 ± 0.3	—	—	—	1.31 ± 0.01

[a] Quantified by ICP-OES. [b] Quantified by ISEF. [c] Quantified by TGA.

The crystalline Cit-ACP-4 sample has a notably lower content of carbonate in comparison with the other samples, and its TGA curve is more complex and presents multiple thermal events in the range of 600–1000 °C (Fig. S3, ESI†). It is likely that Cit-ACP-4 does not only contain carbonate ions but also carbon, as proven by its darker color (Fig. S4, ESI†). The incorporation of a carbonaceous phase into the particles is due to the incomplete oxidation of citrate and carbonates during calcination, which may have been caused by the lower SSA_{BET} of the Cit-ACP-4 sample. In this respect, the possibility of forming bioceramic/graphitic composite materials is an interesting concept emerging from these findings and will be investigated in more detail in the future.

The morphology of the calcined samples was analyzed using FEG-SEM. In Fig. 8 and in Table 4 the representative micrographs as well as the typical particle morphologies and dimensions for each sample are reported. Cit-ACP-4 (Fig. 8A) is composed of spherical particles with a morphology similar to the pristine material,[38] and has a low degree of particle sintering. Apart from some bigger grains, the particle size is between 60 and 120 nm in diameter. On the contrary, Cit-ACP-2 particles

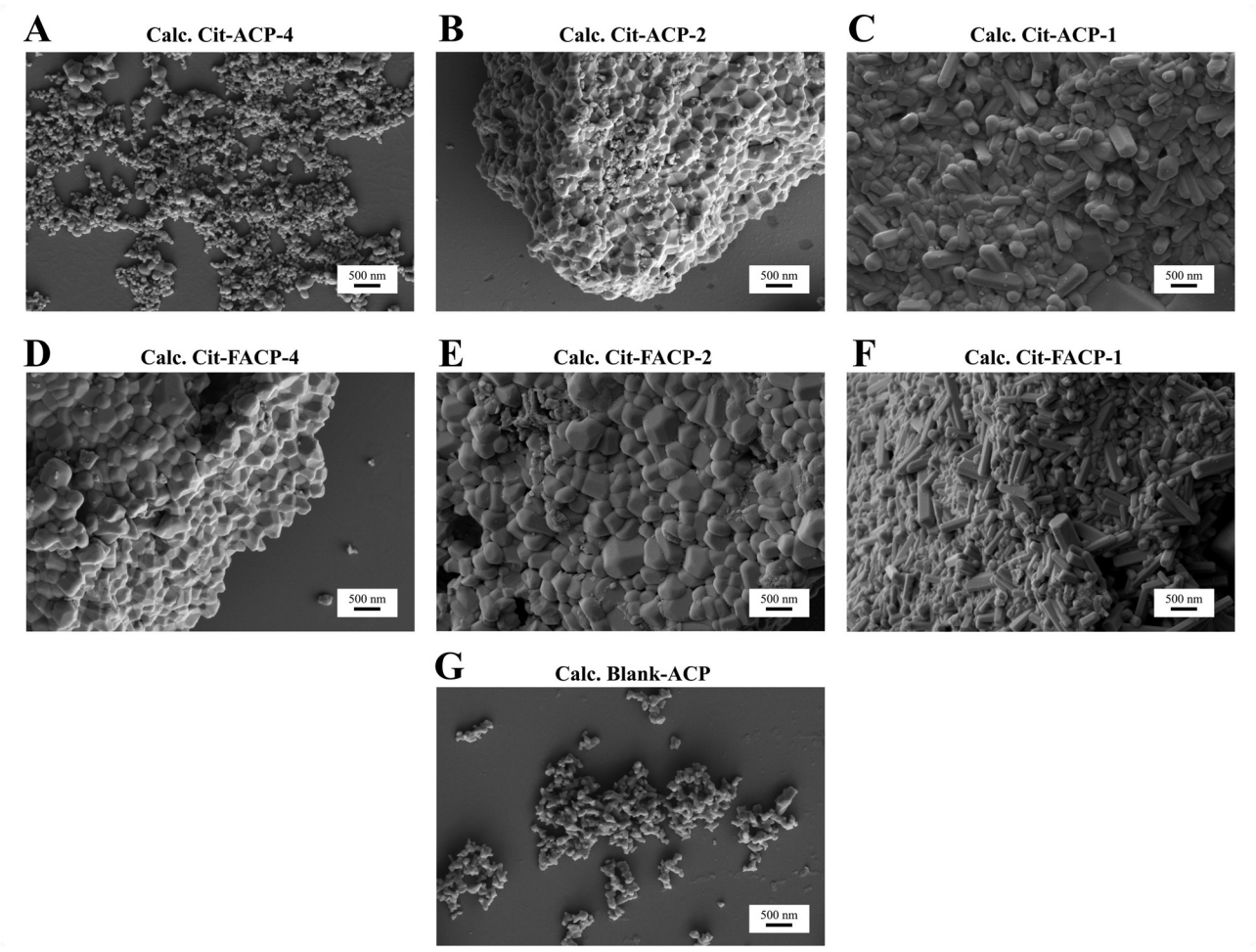

Fig. 8 FEG-SEM micrographs of calcined samples.

Table 4 Morphology and dimensions of calcined samples

Sample	Main particle morphology	Average dimensions (nm)
Calc. Cit-ACP-4	Spherical	60–120
Calc. Cit-ACP-2	Squared	200–400
Calc. Cit-ACP-1	Hexagonal rod	400–1000 (length) 200–350 (width)
Calc. Cit-FACP-4	Squared	300–500
Calc. Cit-FACP-2	Squared	350–600
Calc. Cit-FACP-1	Hexagonal rod	300–1000 (length) 150–250 (width)
Calc. blank-ACP	Irregular	100–150

(Fig. 8B) are bigger and partially sintered, with dimensions between 200 and 400 nm in diameter. Cit-ACP-1 particles (Fig. 8C) are not only bigger than the other Cit-ACP samples, but also present a different morphology, comprising hexagonal rods, with diameters in the 150–250 nm range and lengths that span from 400 nm to 1 μm. Clearly, with the reduction of the Cit/Ca ratio, the crystal growth becomes less hindered in the direction of assuming the hexagonal symmetries of HA.

The morphology of the Cit-FACP-4 and Cit-FACP-2 (Fig. 8D and E) particles is similar to Cit-ACP-2, with fused grains having diameters between 300 and 500 nm for Cit-FACP-4 and between 350 and 600 nm for Cit-FACP-2. Cit-FACP-1 particles (Fig. 8F) are similar to Cit-ACP-1 particles, since both take the form of hexagonal rods with a diameter in the 200–350 nm range and lengths that range from 300 nm to 1 μm. The crystalline rods of Cit-ACP-1 and Cit-FACP-1 are very similar to calcined HA particles reported in the literature, where the morphology reflects the hexagonal crystalline system of HA.[65,66] Finally, the blank-ACP sample (Fig. 8G) is composed of small and irregular particles that are partially fused together and have diameters in the range of 100–150 nm.

To assess the absence of toxicity of the crystalline samples, an *in vitro* study was performed evaluating the viability, proliferation, and morphology of MSCs in contact with them. A quantitative comparative analysis of all the calcined samples at different time points is presented in Fig. 9, showing the percentage of viable cells relative to the cell only control. MTT assay is one of the most frequently used methods for evaluating cell proliferation and cytotoxicity and is based on the reduction of the tetrazolium salt by mitochondrial dehydrogenases of actively growing cells. This assay quantifies the metabolic activity of the cells and is an indirect measure of cell viability, and thus of potential cytotoxic effects exerted by the materials.[67,68] All the samples show a slight time- and dose-dependent cytotoxicity, including calcined blank-ACP, which is known to be a non-cytotoxic material.[69] In fact, the percentage of live cells at the higher particle concentrations (*i.e.*, 200 and 500 μg mL^{-1}) decreased at day 7 compared to the cells only, without significant differences among the samples. The decreasing cell viability observed at day 7 can be ascribable to the effects of the long-term culture in a limited culture area with the presence of a relatively concentrated material. The ANOVA variance analysis, used to compare the effect of the two groups of samples (Cit-ACP *vs.* Cit-FACP), showed that at day 3, the Cit-FACP group significantly decreased the cell viability at 100, 200 and 500 μg mL^{-1} (p-value < 0.05 or less). This specific cellular response for this set of samples is probably induced by the presence of higher quantities of CaO rapidly converting to $Ca(OH)_2$, which is a material known to be cytotoxic due to its basification effect on the media.[70]

Looking at the differences between the cells grown for 3 days with the higher doses of the materials (200 and 500 μg mL^{-1}), it can be concluded that all the Cit-FACP samples induce a slight, statistically significant decrease of cell viability compared to Blank-ACP (p-value < 0.01 or less). In addition, the Cit-ACP group at 500 μg mL^{-1} showed a slight statistical increase of toxicity compared to calcined blank-ACP (p-value < 0.01 or less), but with a lower effect compared to that of the Cit-FACP group. Finally, it is possible to observe a well-defined trend relative to the effect of Cit-ACP-4 on cell viability. In fact, starting from the concentration of 100 μg mL^{-1}, Cit-ACP-4 seems to exert an inductive effect compared to the other Cit-ACP samples at days 1 and 3 of culture, and this trend becomes statistically different when the cells were grown for 1 day with the dose of 500 μg mL^{-1}. As shown in Fig. 9, the viability of cells treated with Cit-ACP-4 is statistically different when compared with the viability of Cit-ACP-2 and Cit-ACP-1 treatment, with p-values less than 0.05. This result agrees with the compositional data, as Cit-ACP-4 is composed of pure HA, without any traces of CaO.

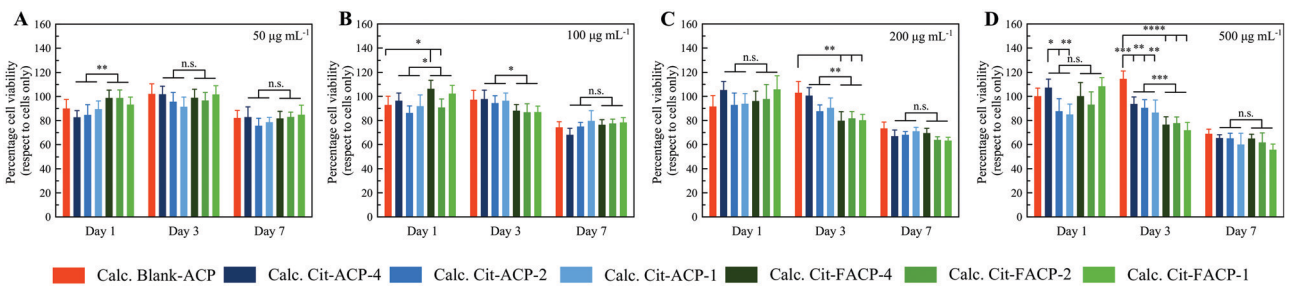

Fig. 9 MSCs viability analysis. MTT assay was performed after 1, 3 and 7 days of culture. The data show the percentage of viable cells as compared to cells only as the control, and the mean ± standard error of the mean are presented. The graphs show the viability of cells grown with (A) 50, (B) 100, (C) 200 and (D) 500 μg mL^{-1} of calcined samples. (*$p \leq 0.05$; **$p \leq 0.01$; ***≤ 0.001; ****$p \leq 0.0001$.)

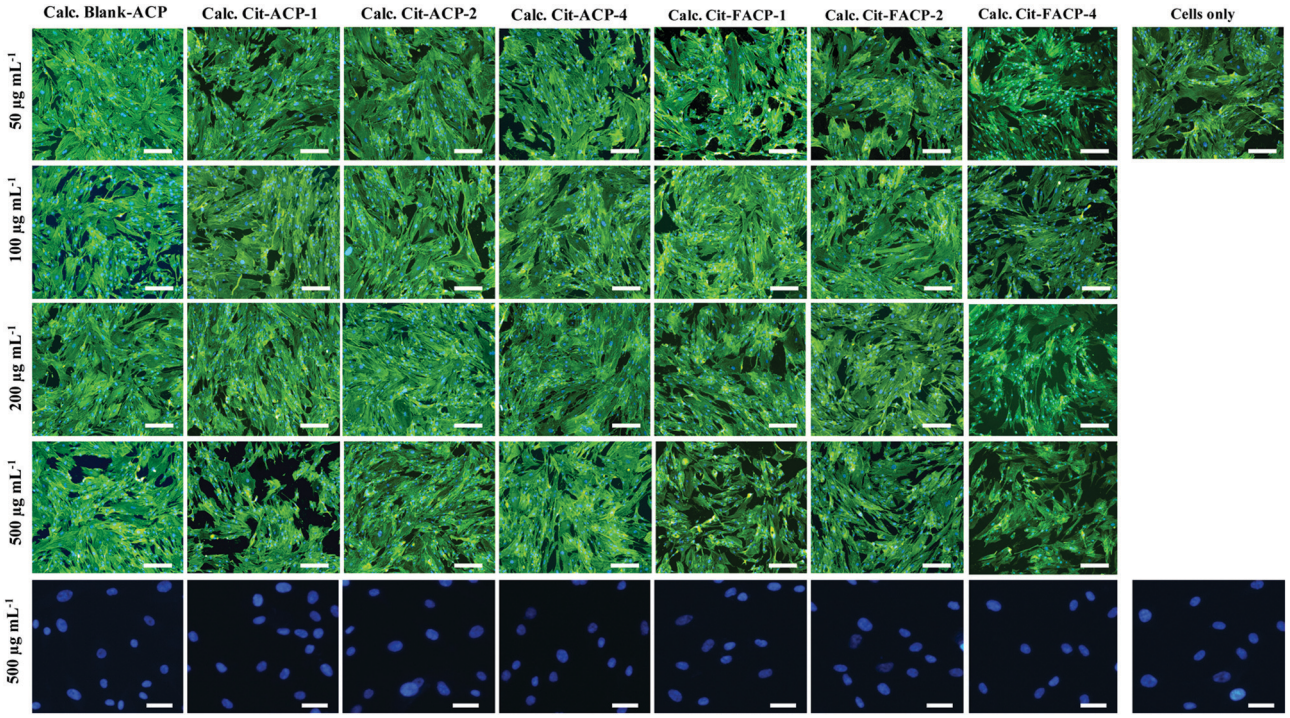

Fig. 10 Morphological analysis of MSCs cultured in the presence of calcined samples at day 2. Phalloidin in green stains for actin filaments and DAPI in blue stains for cell nuclei. Scale bars: 200 μm. A representative image for each sample at a higher concentration shows nuclear morphology (in blue) at the higher magnification. Scale bars: 30 μm.

The morphological evaluation of MSCs grown on the samples after 48 h confirms that only a weak level of dose- and time-dependent cytotoxicity is exerted. Fig. 10 demonstrates that the presence of any of the samples at any of the concentrations tested does not compromise the cytoplasmic and nuclear morphology. The cells are well-spread on the culture plastic surface, showing the typical cytoplasmic elongations without the presence of morphological cell damage markers. Overall, all the biological characterizations prove that all the calcined samples have a good biocompatibility toward MSCs and do not induce any significant cytotoxic responses.

Conclusions

In this work we have studied the thermal crystallization of Cit-(F)ACP samples and citrate-free blank-ACP with calorimetric and other analytical techniques and we have characterized the obtained crystalline products. The influence of the nominal Cit/Ca ratio of the precursors and of fluoride doping were analyzed. We have demonstrated that the thermal crystallization of Cit-ACP is remarkably different from the standard ACP materials (*i.e.*, blank-ACP). First, the crystallization is more favored in Cit-(F)ACP, as these samples have a lower crystallization E_a in comparison to that of blank-ACP. In addition, E_a of crystallization is influenced by the nominal Cit/Ca molar ratio. Citrate mainly regulates the surface area of the materials; however, the relationship between SSA_{BET} and E_a is complex, as in Cit-ACP samples there is a direct correlation between the SSA_{BET} and E_a, whereas in Cit-FACP there is no clear correlation. Considering the Avrami exponents, it is likely that in the Cit-ACP samples the process is more diffusion-controlled and dependent on microstructural effects, while in the Cit-FACP samples the process is more complex and surface-dependent. Secondly, we have discovered that the heat treatment of Cit-(F)ACP at 800 °C yields (F)HA as the main product instead of TCP and calcium pyrophosphate, which are instead produced by the thermal treatment of blank-ACP. The formation of (F)HA is induced by the Ca/P ratio of Cit-(F)ACP samples, which is similar to the Ca/P ratio of HA and different from the ratio of TCP. In the case of the Cit-ACP samples, HA was the only product, while for Cit-FACP samples a small amount of CaO formed alongside FHA. The study of the crystalline products has evinced that (F)HA retains carbonate ions in the crystal structure despite the heat treatment at 800 °C that should have induced decarbonation. Furthermore, the morphology of the calcined products was influenced by the nominal Cit/Ca ratio and by fluoride doping, ranging from rounded nanoparticles to micrometric hexagonal rods. In addition, all the samples were biocompatible and non-cytotoxic, with minimal reductions in the viability of MSCs evident only at the highest concentrations tested ($\geq$200 μg mL^{-1}) and for prolonged incubation times ($>$7 days). Overall, we have previously demonstrated that Cit-(F)ACP is an excellent biomaterial for dental remineralization due to its capability to attach to dental surfaces and to crystallize into (F)HA in the oral environment. In this work we have discovered that the thermal crystallization of Cit-(F)ACP is a complex physical process, highly dependent on the presence of foreign

additives (citrate and fluoride) and leading to interesting products different from the ones reported in the literature. We envisaged that thermal crystallization of Cit-(F)ACP nanoparticles could be a simple and straightforward method to produce advanced bioactive (F)HA based ceramics for different medical applications such as generation of coating for metallic prosthesis and dense or porous three-dimensional scaffolds. Indeed, the preservation of carbonate content, the limited grain growth and the possibility to maintain foreign ions in the structure are interesting properties of HA ceramics that are not easily achievable and up to date require special unconventional treatments such as sintering under CO_2 flow, spark plasma sintering, or cold pressing.[9,63,71]

Author contributions

L. Degli Esposti: conceptualization, investigation, visualization, writing – original draft, writing – review & editing; S. Markovic: investigation, writing – review & editing; N. Ignjatovic: investigation, writing – review & editing; S. Panseri: investigation, writing – review & editing; M. Montesi: investigation, writing – review & editing; A. Adamiano: investigation, writing – review & editing; M. Fosca: investigation, writing – review & editing; J. V. Rau: investigation, writing – review & editing; V. Uskoković: conceptualization, investigation, formal analysis, supervision, writing – original draft, writing – review & editing; M. Iafisco: conceptualization, supervision, writing – original draft, writing – review & editing.

Conflicts of interest

There are no conflicts to declare.

Acknowledgements

This work was supported by the Italian Ministry of Health (Bando Ricerca Finalizzata 2016, no. GR-2016-02364704).

References

1 C. Combes and C. Rey, *Acta Biomater.*, 2010, **6**, 3362–3378.
2 S. V. Dorozhkin, *Acta Biomater.*, 2010, **6**, 4457–4475.
3 F. Betts and A. S. Posner, *Mater. Res. Bull.*, 1974, **9**, 353–360.
4 A. S. Posner, F. Betts and N. C. Blumenthal, *Prog. Cryst. Growth Charact.*, 1980, **3**, 49–64.
5 L. Wang, S. Li, E. Ruiz-Agudo, C. V. Putnis and A. Putnis, *CrystEngComm*, 2012, **14**, 6252–6256.
6 E. Eanes, *Calcif. Tissue Res.*, 1970, **5**, 133–145.
7 S. V. Dorozhkin, *Prog. Biomater.*, 2016, **5**, 9–70.
8 Y. Li, F. Kong and W. Weng, *J. Biomed. Mater. Res., Part B*, 2009, **89**, 508–517.
9 C. Ortali, I. Julien, M. Vandenhende, C. Drouet and E. Champion, *J. Eur. Ceram. Soc.*, 2018, **38**, 2098–2109.
10 A. S. Posner and F. Betts, *Acc. Chem. Res.*, 1975, **8**, 273–281.
11 V. Uskokovic, *Cryst. Growth Des.*, 2019, **19**, 4340–4357.
12 J. Zhao, Y. Liu, W.-B. Sun and H. Zhang, *Chem. Cent. J.*, 2011, **5**, 1–7.
13 M. Hannig and C. Hannig, *Nat. Nanotechnol.*, 2010, **5**, 565–569.
14 M. A. S. Melo, S. F. F. Guedes, H. H. K. Xu and L. K. A. Rodrigues, *Trends Biotechnol.*, 2013, **31**, 459–467.
15 J. Zhao, Y. Liu, W.-B. Sun and X. Yang, *J. Dent. Sci.*, 2012, **7**, 316–323.
16 C. Robinson, R. C. Shore, S. R. Wood, S. J. Brookes, D. A. M. Smith, J. T. Wright, S. Connell and J. Kirkham, *Connect. Tissue Res.*, 2003, **44**, 65–71.
17 E. Beniash, R. A. Metzler, R. S. Lam and P. Gilbert, *J. Struct. Biol.*, 2009, **166**, 133–143.
18 J. Mahamid, B. Aichmayer, E. Shimoni, R. Ziblat, C. Li, S. Siegel, O. Paris, P. Fratzl, S. Weiner and L. Addadi, *Proc. Natl. Acad. Sci. U. S. A.*, 2010, **107**, 6316–6321.
19 A. L. Boskey and A. S. Posner, *J. Phys. Chem.*, 1973, **77**, 2313–2317.
20 S. Liu, W. Weng, Z. Li, L. Pan, K. Cheng, C. Song, P. Du, G. Shen and G. Han, *J. Mater. Sci.: Mater. Med.*, 2009, **20**, 359.
21 E. Eanes and A. Posner, *Calcif. Tissue Res.*, 1968, **2**, 38–48.
22 N. Döbelin, T. J. Brunner, W. J. Stark, M. Eggimann, M. Fisch and M. Bohner, *Calcif. Tissue Res.*, 1968, (2), 38–48.
23 R. Kumar, P. Cheang and K. Khor, *Acta Mater.*, 2004, **52**, 1171–1181.
24 P. Layrolle and A. Lebugle, *Chem. Mater.*, 1994, **6**, 1996–2004.
25 P. Layrolle, A. Ito and T. Tateishi, *J. Am. Ceram. Soc.*, 1998, **81**, 1421–1428.
26 Y. Li, W. Weng and K. C. Tam, *Acta Biomater.*, 2007, **3**, 251–254.
27 M. Maciejewski, T. J. Brunner, S. F. Loher, W. J. Stark and A. Baiker, *Thermochim. Acta*, 2008, **468**, 75–80.
28 S. Somrani, C. Rey and M. Jemal, *J. Mater. Chem.*, 2003, **13**, 888–892.
29 V. Uskoković, S. Marković, L. Veselinović, S. Škapin, N. Ignjatović and D. P. Uskoković, *Phys. Chem. Chem. Phys.*, 2018, **20**, 29221–29235.
30 L. Sinusaite, A. Kareiva and A. Zarkov, *Cryst. Growth Des.*, 2021, **21**(2), 1242–1248.
31 C. Feng, K. Khor, S. Kweh and P. Cheang, *Mater. Lett.*, 2000, **46**, 229–233.
32 K. A. Gross, V. Gross and C. C. Berndt, *J. Am. Ceram. Soc.*, 1998, **81**, 106–112.
33 P. Layrolle and A. Lebugle, *Chem. Mater.*, 1996, **8**, 134–144.
34 Y. Li, D. Li and W. Weng, *Int. J. Appl. Ceram. Technol.*, 2008, **5**, 442–448.
35 E. C. Reynolds, *Spec. Care Dentist.*, 1998, **18**, 8–16.
36 X. Yang, B. Xie, L. Wang, Y. Qin, Z. J. Henneman and G. H. Nancollas, *CrystEngComm*, 2011, **13**, 1153–1158.
37 C. Berg and H.-G. Tiselius, *Urol. Res.*, 1989, **17**, 167–172.
38 M. Iafisco, L. Degli Esposti, G. B. Ramírez-Rodríguez, F. Carella, J. Gómez-Morales, A. C. Ionescu, E. Brambilla, A. Tampieri and J. M. Delgado-López, *Sci. Rep.*, 2018, **8**, 17016.
39 K. Onuma and M. Iijima, *Sci. Rep.*, 2017, **7**, 2711.
40 J. M. Hughes, M. Cameron and K. D. Crowley, *Am. Mineral.*, 1989, **74**, 870–876.
41 K. J. Roche and K. T. Stanton, *J. Fluorine Chem.*, 2014, **161**, 102–109.
42 A. Coelho, *Coelho Software*, 2012.
43 J. Vecstaudza and J. Locs, *J. Alloys Compd.*, 2017, **700**, 215–222.

44 R. Sun, M. Åhlén, C.-W. Tai, É. G. Bajnóczi, F. de Kleijne, N. Ferraz, I. Persson, M. Strømme and O. Cheung, *Nanomaterials*, 2020, **10**, 20.
45 K. Chatzipanagis, M. Iafisco, T. Roncal-Herrero, M. Bilton, A. Tampieri, R. Kroger and J. M. Delgado-Lopez, *CrystEngComm*, 2016, **18**, 3170–3173.
46 J. M. Delgado-López, R. Frison, A. Cervellino, J. Gómez-Morales, A. Guagliardi and N. Masciocchi, *Adv. Funct. Mater.*, 2014, **24**, 1090–1099.
47 V. Uskoković, *Rev. J. Chem.*, 2013, **3**, 271–303.
48 V. M. Fokin, J. W. Schmelzer, M. L. Nascimento and E. D. Zanotto, *J. Chem. Phys.*, 2007, **126**, 234507.
49 R. Gelli, M. Tonelli, F. Ridi, M. Bonini, H. M. Kwaambwa, A. R. Rennie and P. Baglioni, *J. Colloid Interface Sci.*, 2021, **589**, 367–377.
50 H. E. Kissinger, *Anal. Chem.*, 1957, **29**, 1702–1706.
51 L. M. Rodríguez-Lorenzo, J. N. Hart and K. A. Gross, *J. Phys. Chem. B*, 2003, **107**, 8316–8320.
52 K. Haberko, M. M. Bućko, J. Brzezińska-Miecznik, M. Haberko, W. Mozgawa, T. Panz, A. Pyda and J. Zarębski, *J. Eur. Ceram. Soc.*, 2006, **26**, 537–542.
53 T. Goto and K. Sasaki, *Ceram. Int.*, 2014, **40**, 10777–10785.
54 L. Jha, S. Best, J. Knowles, I. Rehman, J. D. Santos and W. Bonfield, *J. Mater. Sci.: Mater. Med.*, 1997, **8**, 185–191.
55 L. Rodrıguez-Lorenzo, J. Hart and K. Gross, *Biomaterials*, 2003, **24**, 3777–3785.
56 L. Degli Esposti, A. Adamiano, A. Tampieri, G. B. Ramirez-Rodriguez, D. Siliqi, C. Giannini, P. Ivanchenko, G. Martra, F.-H. Lin, J. M. Delgado-López and M. Iafisco, *Cryst. Growth Des.*, 2020, **20**(5), 3163–3172.
57 A. Antonakos, E. Liarokapis and T. Leventouri, *Biomaterials*, 2007, **28**, 3043–3054.
58 E. Tkalčec, J. Popović, S. Orlić, S. Milardović and H. Ivanković, *Mater. Sci. Eng., C*, 2014, **42**, 578–586.
59 S. Koutsopoulos, *J. Biomed. Mater. Res., Part B*, 2002, **62**, 600–612.
60 N. Rameshbabu, T. S. Kumar and K. P. Rao, *Bull. Mater. Sci.*, 2006, **29**, 611–615.
61 F. Freund and R. M. Knobel, *J. Chem. Soc., Dalton Trans.*, 1977, 1136–1140.
62 J. M. Delgado-López, M. Iafisco, I. Rodríguez, A. Tampieri, M. Prat and J. Gómez-Morales, *Acta Biomater.*, 2012, **8**, 3491–3499.
63 Z. Zyman and M. Tkachenko, *J. Eur. Ceram. Soc.*, 2011, **31**, 241–248.
64 Y. Doi, T. Shibutani, Y. Moriwaki, T. Kajimoto and Y. Iwayama, *J. Biomed. Mater. Res., Part B*, 1998, **39**, 603–610.
65 S. Pramanik, A. S. M. Hanif, B. Pingguan-Murphy and N. A. Abu Osman, *Materials*, 2013, **6**, 65–75.
66 P. Ideia, L. Degli Esposti, C. C. Miguel, A. Adamiano, M. Iafisco and P. C. Castilho, *Int. J. Appl. Ceram. Technol.*, 2021, **18**, 235–243.
67 V. Uskoković and T. A. Desai, *Mater. Sci. Eng., C*, 2014, **37**, 210–222.
68 M. V. Berridge and A. S. Tan, *Arch. Biochem. Biophys.*, 1993, **303**, 474–482.
69 H.-S. Ryu, K. S. Hong, J.-K. Lee, D. J. Kim, J. H. Lee, B.-S. Chang, D.-H. Lee, C.-K. Lee and S.-S. Chung, *Biomaterials*, 2004, **25**, 393–401.
70 B. Alliot-Licht, A. Jean and M. Gregoire, *Arch. Oral Biol.*, 1994, **39**, 481–489.
71 J. Guo, H. Guo, A. L. Baker, M. T. Lanagan, E. R. Kupp, G. L. Messing and C. A. Randall, *Angew. Chem.*, 2016, **128**, 11629–11633.